

Deciphering Metastable Structure Evolution in Voltage Hysteresis of Lithium-Rich Cathodes

Haoyu Xue, Wenguang Zhao, Minzhi Zhan, Dong Zhou, Nian Zhang, Zhefeng Chen, Rui Qi, Mihai Chu, Shunning Li, Jun Wang,* Qi Liu,* Feng Pan,* and Mingjian Zhang*



Cite This: <https://doi.org/10.1021/acsnano.5c20611>



Read Online

ACCESS |

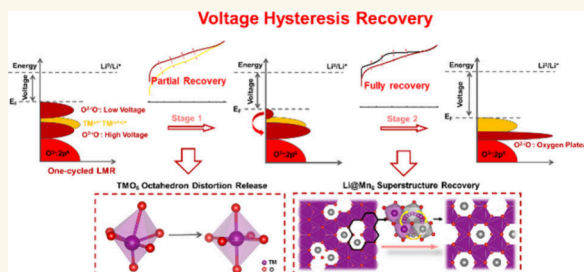
Metrics & More

Article Recommendations

Supporting Information

ABSTRACT: Voltage hysteresis, as one of the main concerns in lithium-rich oxides (LROs), significantly deteriorates the energy conversion efficiency and hinders its application in high-energy-density Li-ion batteries. Nevertheless, the structural origin of voltage hysteresis has still not been clarified. Here we reveal the thermodynamically metastable structure evolution, particularly negative thermal expansion and correlated transition-metal (TM) octahedral (TMO₆) distortion release, during thermally driven voltage hysteresis recovery in LROs. Moreover, whole exothermic structure evolution and related voltage recovery are linked: (1) abnormal negative thermal expansion below 200 °C due to the relief of octahedral distortion, which leads to a voltage recovery by 0.26 V; (2) reconstruction of Li@Mn₆ superstructure units due to Li-vacancy-assisted TM migration at 300 °C, which further recovers the voltage by 0.16 V and the oxygen plateau. Our work provides a more elaborate picture of the structure–voltage correlation in anionic-redox systems and highlights that these two structural variations form a metastable phase, serving as a solid base after the first cycle for subsequent cycling in LROs.

KEYWORDS: voltage hysteresis, thermal treatment, negative thermal expansion, octahedral distortion, TM migration



RESULTS

The working voltage, explained as the potential difference between the cathode and anode, is viewed as one critical determiner of the energy density (defined as an integral of voltage over the specific capacity) in lithium-ion batteries (LIBs). The potential (E), written in eq 1,¹ involves the standard electrode potential (E^0), the Faraday constant (F), and the Gibbs free energy (G) of cathode materials during the Li⁺ extraction/intercalation process.

$$E - E^0 = \frac{G_{\text{cathode}}(\text{lithiated}) - G_{\text{cathode}}(\text{delithiated})}{zF} \quad (1)$$

As widely investigated, this is determined by various structural features of the cathode/anode, including the redox couples,² ligand types,³ site energy of Li⁺ occupation,⁴ crystal phase,⁵ and so on. According to eq 1, lithium-rich oxides (LROs) undergo a serious voltage drop after the first cycle, which means that the cycled material must suffer a significant change in the Gibbs energy compared with the pristine material.

Voltage hysteresis, as one of the main concerns in LROs, would result in a low energy efficiency (<80%) in the LIB.⁶ Based on the law of conservation of energy, the lost energy must be dissipated out of or stored in the LROs material system. The lattice oxygen loss, derived from the thermodynamically unstable crystal oxygen throughout the whole

charge–discharge cycle, may be one form of the energy loss.⁷ Recent work in Chueh's group on the quantitative relationship between oxygen loss and crystal expansion in the first cycle⁸ revealed a serious deviation between the experimentally measured expansion coefficient (0.68) and the theoretical value (0.22). Therefore, there must be other unknown structure changes responsible for the crystal expansion and energy loss due to voltage hysteresis.

Thermodynamically, the lattice changes of the LROs material over the voltage hysteresis are expected to be endothermic due to the lost energy, and, conversely, the recovery to the pristine state is exothermic. Temperature-programmed heating experiments exactly demonstrate that lithium and transition metal (TM) exothermally migrate back to regenerate a Li@Mn₆ superstructure at 300 °C with the assistance of vacancy.^{9–11} Generally accepted, TM irreversible migration would destroy Li@Mn₆ superstructure units during the first cycle of LROs, thus raising the energy of O 2p states and lowering the voltage, eventually causing voltage hyste-

Received: November 25, 2025

Revised: February 6, 2026

Accepted: February 6, 2026

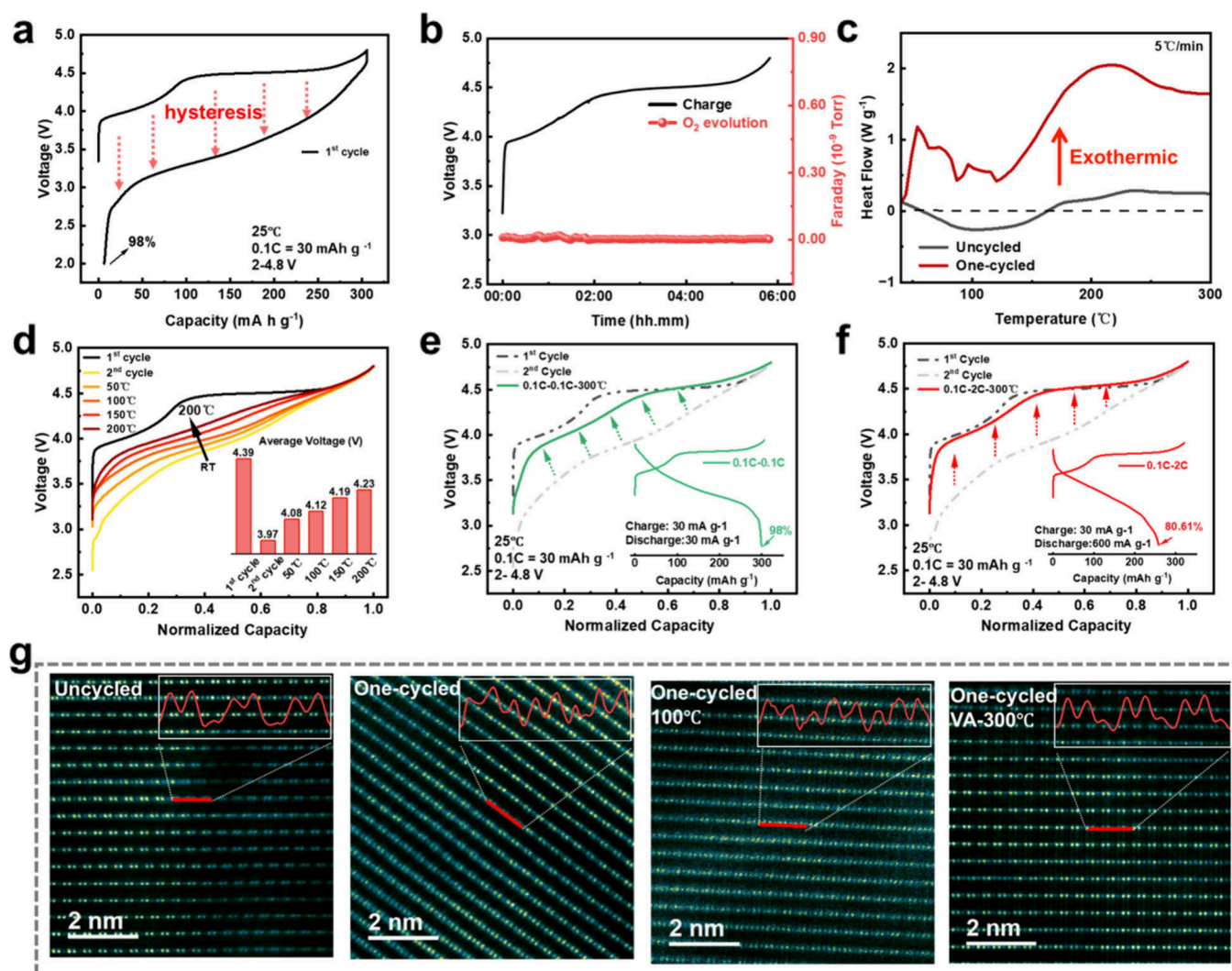


Figure 1. Voltage recovery process and exothermic behaviors. (a) First charge–discharge profile of LMR114. (b) Operando DEMS test during the first charge of LMR114. (c) DSC curves of uncycled LMR114 and one-cycled LMR114. (d) First charge profiles of LMR114 cathodes after vacuum heating treatment at different temperatures. The first and second charge profiles of pristine LMR114 were added for comparison. (e) Charge profile of the LMR114 sample annealed at 300 °C after the first symmetric cycle with a charge and discharge rate of 0.1 C. (f) Charge profile of the LMR114 sample annealed at 300 °C after the first asymmetric cycle with a charge rate of 0.1 C and a discharge rate of 2 C. (g) HAADF-STEM images of pristine LMR114, LMR114 after the first cycle, LMR114 annealed at 100 °C after the symmetric charge–discharge cycle, and LMR114 annealed at 300 °C in a vacuum after the asymmetric charge–discharge cycle, from left to right.

res.^{12–14} Nonetheless, there are other anionic-redox cathodes experiencing reversible/no TM migration but still suffering from serious voltage hysteresis,^{15,16} which hints at the existence of other intrinsic structure changes. Moreover, Meng’s group recently revealed the presence of negative thermal expansion and established its linkage with oxygen-redox electrochemistry in LROs.¹⁷ However, detailed structural changes and a clear illustration of its relationship with voltage are still lacking, calling for further in-depth investigation.

Here we systematically investigated the metastable structure evolution, providing a detailed explanation of the local structural changes and the relationship with voltage during the thermally driven voltage hysteresis recovery of $\text{Li}(\text{Li}_{0.136}\text{Mn}_{0.560}\text{Ni}_{0.147}\text{Co}_{0.156})\text{O}_2$ (LMR114) as a function of the temperature and Li vacancies. Using atom-resolved scanning transmission electron microscopy (STEM), temperature-dependent X-ray diffraction (XRD), and varied-temperature transmission electron microscopy (TEM), the reasonably exothermic voltage recovery process is divided into two stages:

- (1) an unusual negative thermal expansion below 200 °C contributes to a significant voltage recovery of 0.26 V;
- (2) reconstruction of superstructure units with the assistance of Li vacancies at 300 °C further elevates the voltage by 0.16 V and completely recovers the oxygen oxidation plateau. Further studies into the chemical and short-range structural changes by hard and soft X-ray absorption spectroscopy (hXAS and sXAS) and ab initio molecular dynamics (AIMD) illustrate that the unusual negative thermal expansion is attributed to the release of lattice distortion, especially TMO_6 octahedral distortion. These findings stress the role of two types of local structure changes, TM migration and TMO_6 octahedral distortion, in voltage hysteresis and establish a more comprehensive structure–voltage relationship in LMRs.

Exothermic Voltage Recovery of Discharged LMRs

A representative lithium-rich oxide LMR114 was subjected to electrochemical cycling and subsequent vacuum thermal treatment for the voltage recovery process (Figure S1). The

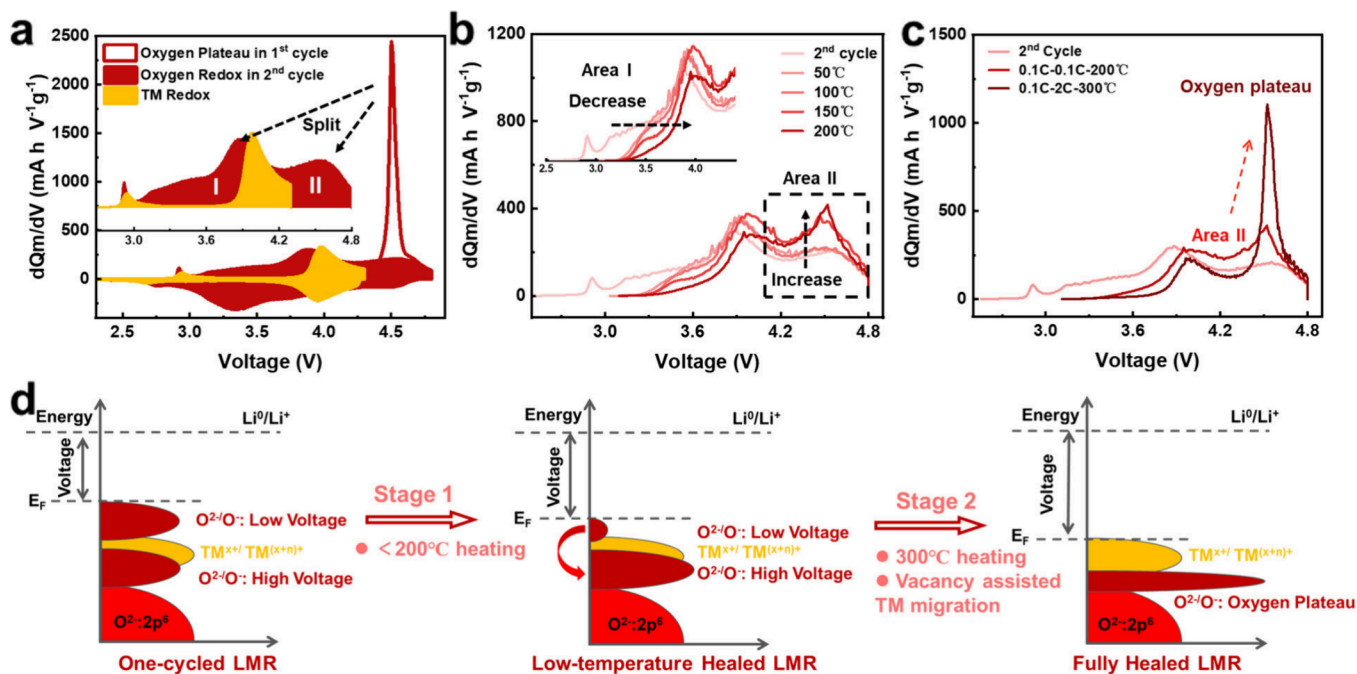


Figure 2. Redox couple evolution during the voltage recovery process with the thermal treatment. (a) dQ/dV curves of LMR114 under the upper cutoff voltages of 4.25 and 4.8 V. Yellow and red shaded regions come from the contributions of TM redox and O redox, respectively. The inset shows the dQ/dV curve of the second charge branch within 2.0–4.8 V. (b) dQ/dV profiles of one-cycled LMR114 samples annealed below 200 °C. The inset shows the evolution of Area I, while the dotted box shows Area II in part a during the thermal process. (c) dQ/dV profile of one-cycled LMR114 samples annealed at 300 °C with two other profiles as a comparison. (d) Schematic redox couple diagram to show the voltage changes of oxygen oxidation during the voltage recovery process, derived from the changes in the corresponding dQ/dV profiles.

inductively coupled plasma atomic emission spectroscopy (ICP-AES) results indicate that LMR114 owns a typical chemical formula of $\text{Li}(\text{Li}_{0.136}\text{Mn}_{0.560}\text{Ni}_{0.147}\text{Co}_{0.156})\text{O}_2$ (Table S1). The scanning electron microscopy (SEM) and energy-dispersive X-ray spectroscopy (EDS) characterization depicts the spherical morphology of secondary particles and the uniform distribution of Mn, Ni, Co, and O elements (Figure S2). Rietveld refinement was conducted on the XRD pattern with a typical layered phase (space group $R\bar{3}m$; Figure S3 and Tables S2 and S3). The high-angle annular dark-field scanning transmission electron microscopy (HAADF-STEM) image along the $[1-10]$ direction (Figure S4c) exhibits two distinctive domains of Li_2MnO_3 (featuring the bright–bright–dark... pattern) and LiTMO_2 (featuring the bright–bright–bright... pattern). The first charge–discharge tests (Figures 1a and S5) and differential electrochemical mass spectrometry (Figure 1b) demonstrate that a high initial Coulombic efficiency of LMR114 (up to 98%) and no obvious O_2 release, which show negligible Li loss and oxygen loss. Most interestingly, even with a negligible change of the chemical composition, LMR114 still suffers from serious voltage hysteresis and a low energy efficiency (79%) (1342 Wh kg^{-1} input and 1061 Wh kg^{-1} output), which can exclude the influence of the chemical composition change in voltage hysteresis.

As depicted in Figures S6 and S7, we performed a vacuum heating treatment on the one-cycled LMR114 cathodes using vacuum-sealed quartz glass tubes at different temperatures. The differential scanning calorimetry (DSC, Figure 1c) tests indicate that one-cycled LMR114 exhibits exothermic behavior during the heating treatment, which corresponds to the release of energy stored in the lattice structure due to the voltage hysteresis. The charge–discharge profiles after heating treat-

ment show apparent voltage recovery with the increased temperature (Figures 1d, S8, and S9), from 3.97 to 4.08 (50 °C), 4.12 (100 °C), 4.18 (150 °C), and 4.23 V (200 °C), which is gradually close to the initial charging voltage of 4.39 V. Because the heating treatment was conducted in a vacuum, TM oxidation barely occurs, which excludes the effect of TM oxidation on the voltage recovery. Notably, ~ 0.11 V of the voltage recovery occurred at the very low temperature of 50 °C. At such a low temperature, atom migration in the lattice is impossible, which excludes the effect of TM migration. When the healing temperature was elevated to 300 °C (Figure 1e), the entire charge profile displays a diagonal upward trend along the direction of the arrows, while the oxygen oxidation plateau still has not been fully recovered. This phenomenon is inconsistent with the previous reports because Meng's group¹⁰ and Indris's group¹¹ achieved full recovery of the oxygen oxidation plateau at 300 °C. Considering that the oxygen oxidation plateau is highly correlated with the Li@Mn_6 superlattice units, it is reasonable to believe that fully recovering the oxygen oxidation plateau requires healing of the damaged Li@Mn_6 superlattice units.¹³ The previous reports indicate that the existence of the vacancy facilitates TM migration for reconstructing superstructure units.¹⁸ One-cycled LMR114 has bare vacancy due to the high Coulombic efficiency (98%), which is harmful to the reconstruction of superstructure units. To produce Li vacancies, we designed an asymmetric charge–discharge strategy (0.1C current rate charging and 2C rate discharging with a Coulombic efficiency of 80.61%; inset of Figure 1f). Eventually, after the same thermal treatment at 300 °C, the charge profile and oxygen oxidation plateau basically reach complete recovery (Figures 1f and S10).

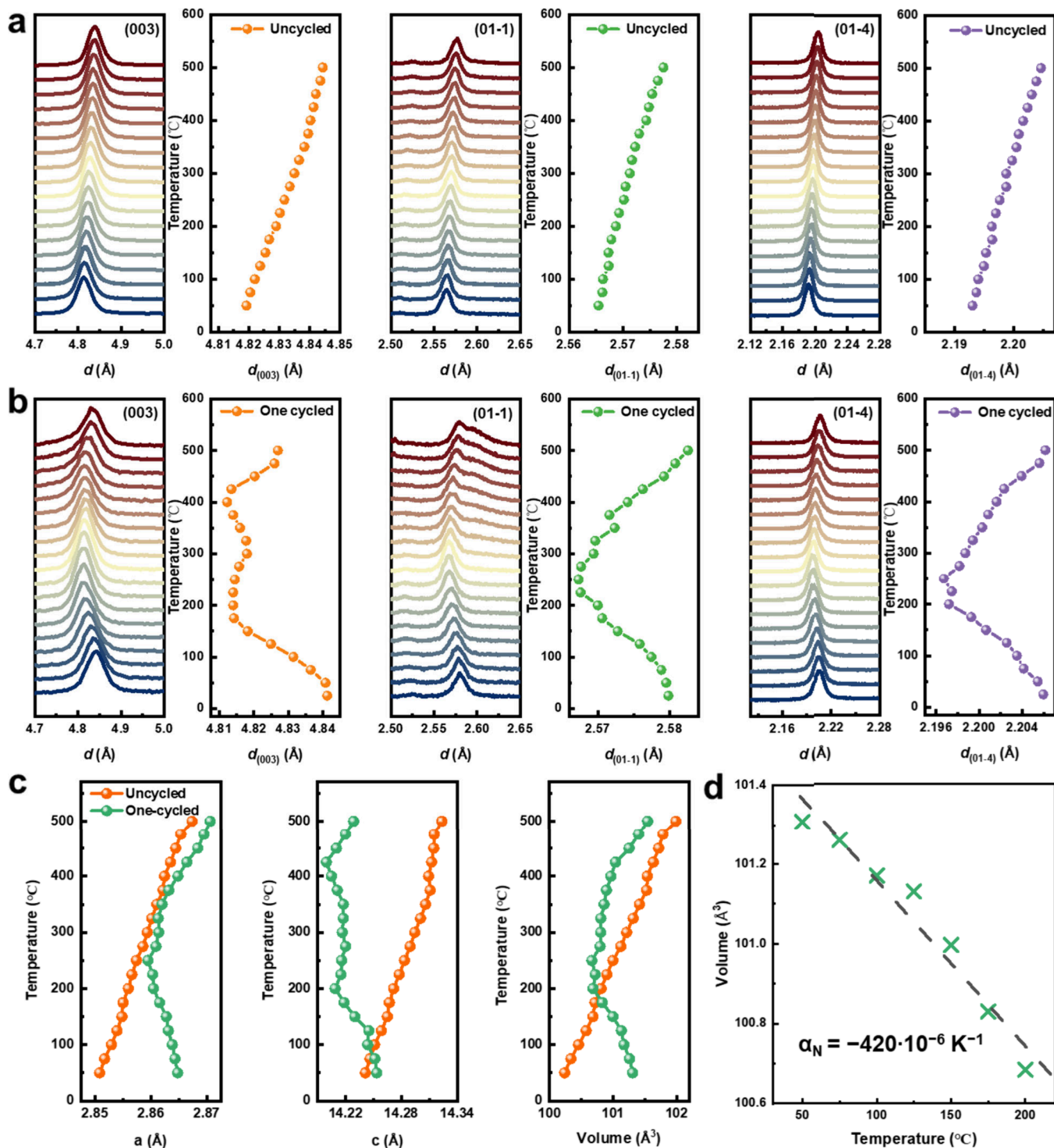


Figure 3. Long-range structure change during the thermal treatment for voltage recovery. (a and b) Evolution of the (003), (01–1), and (01–4) peaks for pristine LMR114 (a) and one-cycled LMR114 (b) during the thermal treatment up to 500 °C with a ramping rate of 10 °C/min. The corresponding interplanar spacings were plotted as a function of the temperature. (c) Plots of the lattice parameters as a function of the temperature. (d) Linear fitting between the lattice volume and temperature for one-cycled LMR114 below 200 °C.

To track the structural changes during the exothermic healing process, atom-resolved HAADF-STEM images of LMR114 in different states were collected. As shown in Figure 1g, pristine LMR114 presents a regular “bright–bright–dark...” pattern in TM layers, representing the typical “Mn–Mn–Li” arrangement from Li@Mn₆ superstructure units. After the first cycle, the pattern evolves to “bright–bright–slightly bright...”.

This indicates the damage of Li@Mn₆ superstructure units due to TM migration, consistent with the disappearance of superlattice peaks in the XRD pattern after the first cycle (Figure S11). When the sample was annealed at 100 °C after a symmetric charge–discharge cycle, the “bright–bright–slightly bright...” pattern is still maintained, indicating that the Li@Mn₆ superstructure units are not recovered. This hints at other

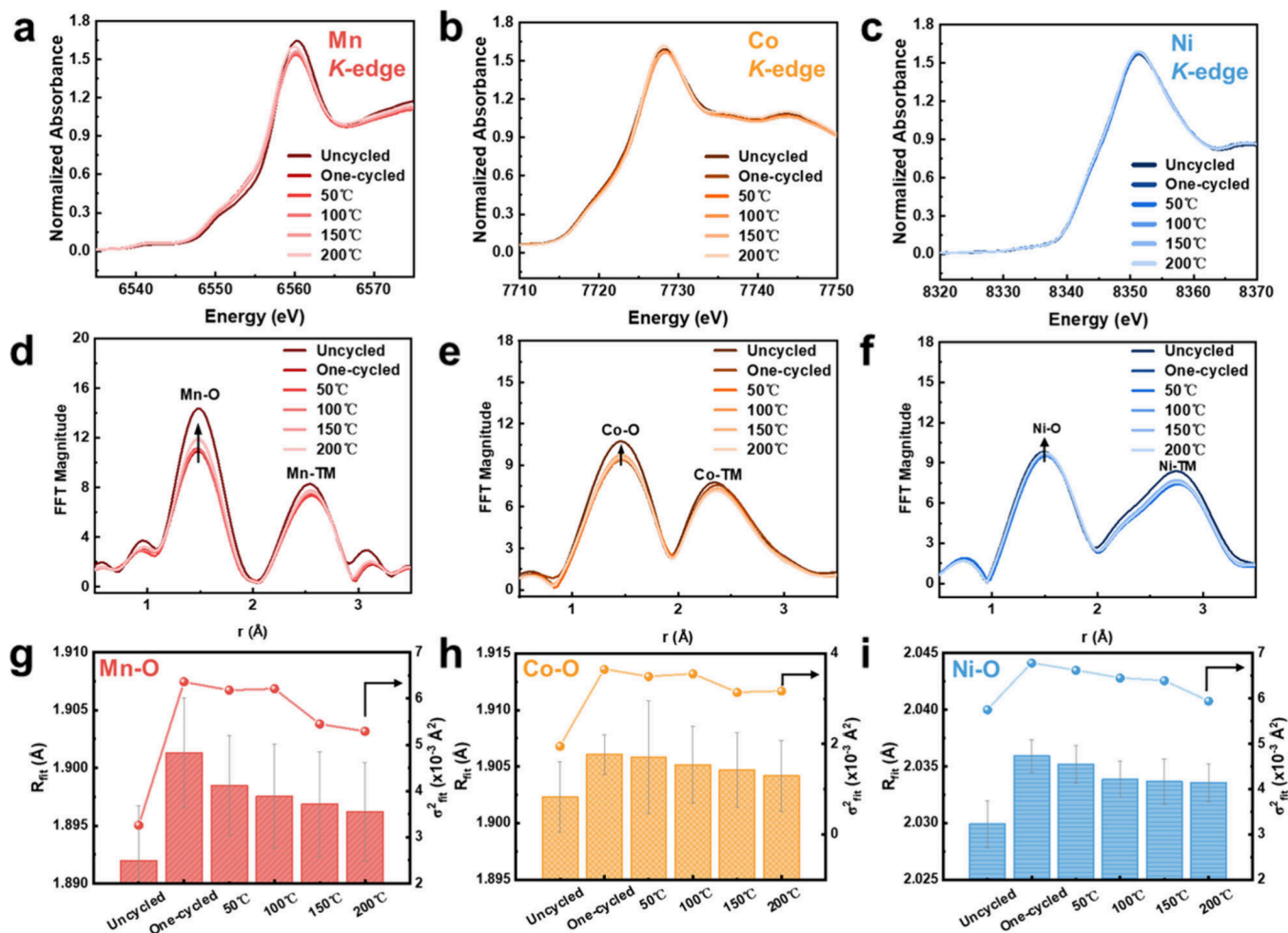


Figure 4. Short-range structure changes during negative thermal expansion. Mn (a), Co (b), and Ni (c) K-edge XANES spectra of uncycled and one-cycled LMR114 after heating treatment at different temperatures. Mn (d), Co (e), and Ni (f) EXAFS spectra of uncycled and one-cycled LMR114 after heating treatment at different temperatures. The bond length and structure disorder factor (σ^2) of Mn–O (g), Co–O (h), and Ni–O (i) bonds for uncycled and one-cycled LMR114 after heating treatment at different temperatures.

structure changes being responsible for the voltage recovery by 0.15 V after heating above 100 °C. In comparison, the sample annealed at 300 °C with vacancy assistance presents a well-defined “bright–bright–dark...” pattern in TM layers, confirming the recovery of superstructure units. This is further validated by the reappearance of the typical superlattice peak near 21° in the XRD pattern (Figure S11).

To figure out how the voltage recovery proceeds, a detailed dQ/dV profile analysis was conducted on one-cycled LMR114 after thermal treatment at different temperatures. As shown in Figure 2a, the second charge profile can be divided into three areas, one yellow-shaded area and two red-shaded areas (low-voltage broad Area I and high-voltage broad Area II).¹⁹ The yellow-shaded area comes from TM oxidation, while the two red-shaded areas arise from lattice oxygen oxidation, evolving from the narrow oxygen oxidation plateau peak in the first cycle. As shown in Figure 2b, the thermal treatment below 200 °C gradually decreases Area I and increases Area II, which leads to the average voltage increase but no oxygen plateau recovery. Further annealing at 300 °C with the assistance of Li vacancies transforms the broad Area II to the narrow oxygen plateau (Figure 2c) because the Li@Mn₆ superstructure is reconstructed.

Based on these results, the voltage recovery process can be divided into two stages (Figure 2d): (1) during heat treatment below 200 °C, the charge profile shows gradual voltage recovery but negligible healing of the oxygen oxidation plateau, corresponding to the transition of the low-voltage O²⁻/O⁻ redox couple to the high-voltage O²⁻/O⁻ redox couple; (2) after thermal treatment at 300 °C with Li-vacancy assistance, the charge profile is fully recovered, especially with the oxygen oxidation plateau, corresponding to the disappearance of the low-voltage O²⁻/O⁻ redox couple and the narrowing of the high-voltage O²⁻/O⁻ redox couple. It is intuitive that Li-vacancy-assisted TM migration restores the Li@Mn₆ superstructure units, thereby contributing to the recovery of the oxygen oxidation plateau (Figures 1f and S12). In contrast, the calculated diffusion energy barrier for Mn migration without Li-vacancy assistance is significantly higher, reaching 3.5 eV, approximately twice that of the Li-vacancy-assisted scenario, which highlights the difficulty of Mn migration back to its original position in stage 1 (Figure S13). Consequently, the thermodynamic changes in the metastable structure that contribute to voltage recovery in stage 1 warrant further investigation.

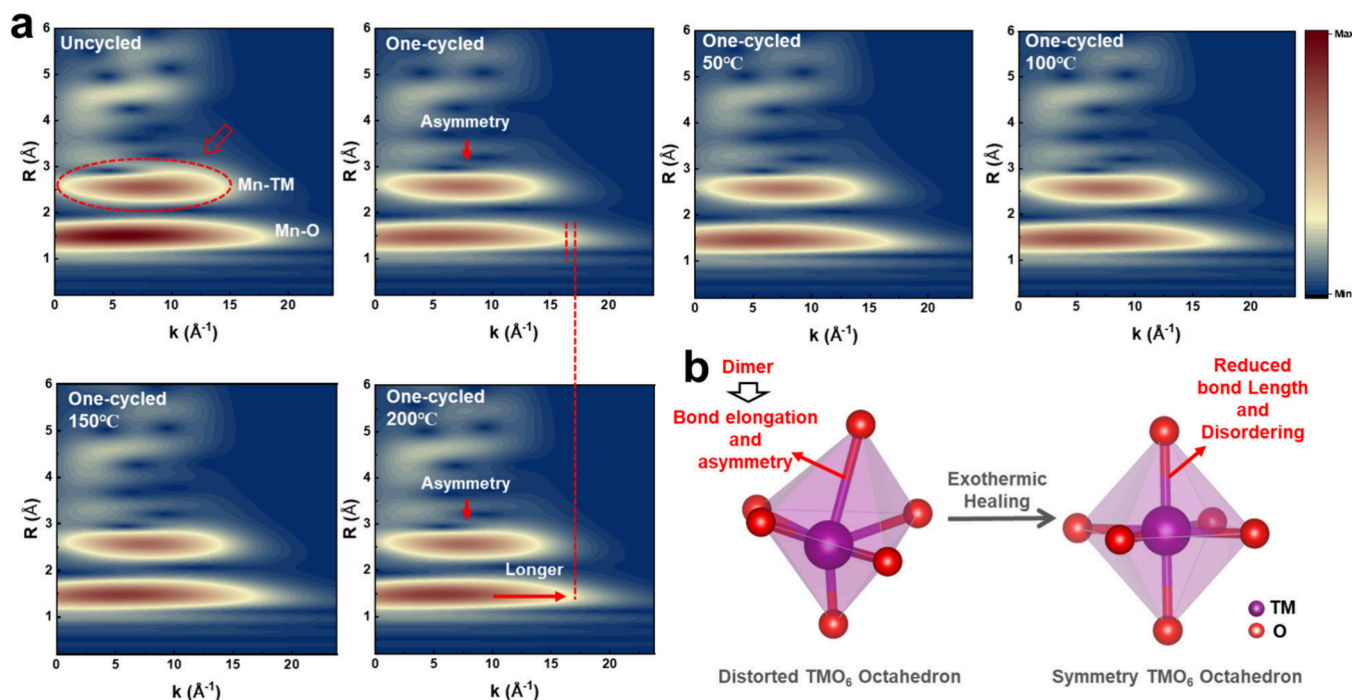


Figure 5. Visualization of the local structure evolution during negative thermal expansion. (a) Wavelet transform analyses on the Mn EXAFS of the pristine LMR114, one-cycled LMR114, and one-cycled LMR114 samples after heating treatment at different temperatures. The unified color intensity is the magnitude of the wavelet transform modulus, which is related to decomposition of the EXAFS amplitude term.²⁸ (b) Scheme illustrating the relief of TMO_6 octahedral distortion during the exothermic healing process. Upon dimerization, the O–O pair distance decreases from ~ 2.8 to ~ 1.46 Å (peroxide)⁴¹ or ~ 1.2 Å (molecular oxygen).¹⁴ This charge-driven dimerization induces severe distortions, including bond elongation and asymmetry, which remain unreleased during discharge. The thermal energy drives the relaxation of TMO_6 octahedra, reducing bond lengths and structural disorder, which subsequently results in exothermic heat release and negative thermal expansion.

Negative Thermal Expansion during Voltage Recovery

To clarify the long-range structural changes coupling the exothermic healing process, temperature-dependent XRD was first performed during the heating treatment of one-cycled LMR114 cathodes (Figure 3b). A similar experiment was performed on the pristine LMR114 cathode for comparison (Figure 3a). As shown in Figure 3a, the main peaks (003), (01–1), and (01–4) continuously shift to the low interplanar spacing (d) as the temperature increases, showing a linear relationship between the d value and temperatures below 500 °C. This indicates a typical lattice thermal expansion behavior, and no other structure changes in the pristine cathode. In contrast, the one-cycled LMR114 cathode exhibits completely different peak shift behaviors (Figure 3b). The plots of the corresponding interplanar spacings versus temperature indicate lattice shrinkage below 200 °C and lattice expansion at higher temperatures ($d_{(003)}$ above 400 °C and $d_{(01-1)}$ and $d_{(01-4)}$ above 300 °C), which is obviously different from the linear thermal expansion behavior in pristine LMR114. In Figure 3c, the lattice parameters a and c and cell volume obtained from Rietveld refinement were further plotted as a function of the temperature. This clearly shows a continuous decrease for all three parameters below 200 °C (from 2.865 to 2.860 Å for a , from 14.254 to 14.209 Å for c , and from 101.308 to 100.685 Å³ for the cell volume). We speculate here that such abnormal negative thermal expansion below 200 °C is related with the obvious voltage recovery (0.26 V) below 200 °C and above.

A temperature-resolved TEM study was further performed on a one-cycled LMR114 cathode to track the microscopic structural changes during the heating treatment. As shown in Figure S14, the similar lattice fringes in the high-resolution

TEM images and the similar fast Fourier transform (FFT) maps indicate that no phase transition occurred below 100 °C. The interplanar spacing was determined by the inverse FFT maps in the right panel of Figure S14. It is clear that the (003) interplanar distance decreases from 4.87 and 4.83 to 4.78 Å with temperature, and the (01–1) and (01–4) interplanar distances also exhibit a small decrease from 2.51 to 2.48 Å and from 2.10 to 2.09 Å, respectively. The results are consistent with the temperature-dependent XRD results above, confirming negative thermal expansion at low temperatures. Importantly, the negative thermal expansion observed here is hardly attributed to TM migration, which is proven to need the assistance of Li^+ vacancies above.

Negative thermal expansion has been well investigated in some oxides with a flexibility structure (Table S4). The relationship between the lattice volume and temperature is usually quantified via the thermal expansion coefficient, α_N . After the linear fitting between the lattice volume and temperature (323.15–473.15 K, Figure 3d), a large negative thermal expansion coefficient, α_N , of $-420 \times 10^{-6} \text{ K}^{-1}$ is obtained for one-cycled LMR114. A well-known mechanism for those negative thermal expansion oxides is the transverse vibration of the bridging oxygen atoms (Figure S15).²⁰ However, the transverse vibration of bridging oxygen atoms would cause the end atoms to get close with each other, which should be endothermic because of the high energy cost of stretching interatomic bonds.²¹ This is totally different from the exothermally negative thermal expansion for the one-cycled LMR114 here. Therefore, the large α_N value and corresponding obvious voltage recovery can be attributed to the atom

vibration with energy release; for example, the TM–O bond length and disordering decrease, as proven later.

Short-Range Structure Changes during Negative Thermal Expansion

To check the structural origin of the abnormal negative thermal expansion, XAS and X-ray photoelectron spectroscopy (XPS) were first performed to check the chemical changes of TM and O during the vacuum thermal treatment. The O K-edge sXAS spectra (Figure S16) under the total fluorescence yield (TFY, probing depth of ~150 nm) mode show a negligible difference after treatment, indicating no lattice oxygen redox.²² The Mn, Co, and Ni K-edge X-ray absorption near-edge spectroscopy (XANES; Figures 4a–c and S17) and XPS (Figure S18) results show no change in the peak position after thermal treatment, further confirming that no TM redox is involved inside the particles. All of these results are consistent with the unchanged chemical composition mentioned above and exclude the contribution of the TM/O redox chemistry to the negative thermal expansion and related voltage recovery.

The Mn, Co, and Ni K-edge extended X-ray absorption fine structure (EXAFS) spectra on the cycled LMR114 samples were collected to track the changes in the short-range structure (Figure 4d–f). The EXAFS spectra in *r* space indicate that the Mn–O, Co–O, and Ni–O peaks intensify with temperature upward, and therein the change extent in the Mn–O peak is the biggest, while the changes in Mn–TM, Co–TM, and Ni–TM are mild. The biggest variation in the Mn–O peak depicts that the structural change in the TM first shell range occurs preferentially around Mn.²³ Unlike Co and Ni, the Mn cations maintain a constant valence state during the first cycle.²⁴ This surely demonstrates that the changes in the Mn–O bond are attributed to oxygen oxidation. EXAFS fitting was further employed for the quantitative analysis (Figures S19–S21 and Tables S5–S7).²⁵ Both the TM–O bond and Debye–Waller factor (σ^2) are pictured as Figure 4g–i. The Debye–Waller factor can be directly used to represent the structural disorder of the TM–O bond.²⁶ As the temperature increases, all of the TM–O bond lengths decrease toward the uncycled state [from 1.901(3) to 1.896(2) Å for Mn–O, from 1.906(1) to 1.904(2) Å for Co–O, and from 2.035(9) to 2.033(6) Å for Ni–O]. The σ^2 value also decreases to the original value of pristine LMR114 (from 6.36 to 5.29 for Mn–O, from 3.65 to 3.17 for Co–O, and from 6.78 to 5.94 for Ni–O). The obvious decrease in the TM–O bond length and disordering can reduce the distance and asymmetry between anions and cations. Because there is no change in the TM valence state, the abnormal negative thermal expansion can be solely attributed to the decrease in the TM–O bond length and disordering, which can be deemed as TMO₆ octahedral distortion.

Further visualization of the local-range structures in the correlated *R*–*k* two-dimensional space was conducted by the Cauchy wavelet transform analysis (Figures 5a and S22–S24).^{27,28} In Figure 5a, an asymmetric ellipse shape of the Mn–TM signal for uncycled LMR114 can be observed, which is correlated to the difference in the next-nearest-neighboring environments of Mn in the Li₂MnO₃ domain and the LiTMO₂ domain (Mn₃Li₃ and TM₆, respectively). After the first cycle, the shape of the Mn–TM signal tends to be more symmetric, which can be explained by the transformation in the nearest neighboring environment to TM_{3+n}Li_{3–n} ($3 \geq n \geq 0$) due to

TM migration and the broken Li@Mn₆ superstructure. After the heating treatments at different temperatures, the Mn–TM signals show similar symmetric shapes, demonstrating that the heating treatments barely affect the next-nearest environment of Mn. In other words, the low-temperature heating cannot drive TM migration back and recover the broken Li@Mn₆ superstructure with no vacancy assistance as proven above (Figure 5b). In contrast, the shape of the Mn–O signal becomes shorter after the first cycle and then gets longer toward the uncycled state with heating temperature (dotted lines in Figure 5a). Moreover, similar changes occur on the highest point of the Mn–O signal in magnitude and *k* space, which decrease after the first cycle and then gradually recover with temperature (Figure S22). These results further exclude TM migration and highlight the relieved TMO₆ octahedral distortion results in the negative thermal expansion and correlated voltage recovery as proven by EXAFS fitting (Figure 5b). Additionally, the obvious changes occur in the *R* range of 4–6 Å of in the Co and Ni EXAFS spectra in correlated *R*–*k* space (Figures S23 and S24), corresponding to the multiple-scattering region involving combined transition metals (e.g., Co–TM–Mn). The gradual recovery of the multiple-scattering peak during the heating process may imply the healing of the MnO₆ octahedra distortion. On the basis of these results, we speculate that the distortion of TM octahedra accompanied by lattice oxygen oxidation occurs during charge, which cannot be fully relieved during the first discharge. The low-temperature (≤ 200 °C) heating can heal such distortion to a large extent, which couples with a significant negative thermal expansion and then leads to the obvious voltage recovery (~0.26 V; Figure 5b).

Residual TMO₆ Octahedra Distortion

To better understand how the relief of TMO₆ octahedra distortion induces negative thermal expansion, we performed an AIMD simulation under 473 K (200 °C) on a Li₂MnO₃ structure model (Figure 6a). As shown in Figures 6a, S25, and S26, once Li₂MnO₃ (State I) is cycled, the lattice O oxidation would induce formation of the O–O dimers, thereby giving rise to serious distortion for the neighboring MnO₆ octahedra (State II) with a great difference in the Mn–O bond lengths.^{16,29} Notably, density functional theory (DFT) calculation results in Figure S25 demonstrate that the bond length between Mn⁴⁺ and O–O dimers varies most [from 1.929(0) to 2.202(0) Å]. The thermal treatment at 473 K can drive the O vibration in cycled Li₂MnO₃, gradually smooth the distortion (State III after 2500 fs), and basically eliminate the distortion of MnO₆ octahedra after 5000 fs (State IV). Two MnO₆ octahedra near the dimerization region were zoomed at the lower panel of Figure 6a. They clearly showcase the gradual decrease in distortion, as traced by blue arrows and evidenced by the decreased Mn–O bond length. The average Mn–O bond lengths for the entire structure from AIMD at different states are summarized in Figure 6b. It increases from 1.930(1) to 1.958(6) Å after the first cycle and then decreases to 1.952(3) Å after the thermal treatment, which shows high consistency with the EXAFS fitting results. In addition, the lattice parameters *a*, *b*, and *c* decrease after the thermal treatment based on the simulation (Figure S27), which is also consistent with the negative thermal expansion observed experimentally above. These results indicate that the thermal treatment can recover the distortion of TMO₆ octahedra accompanied by the shortening of the average TM–O bond

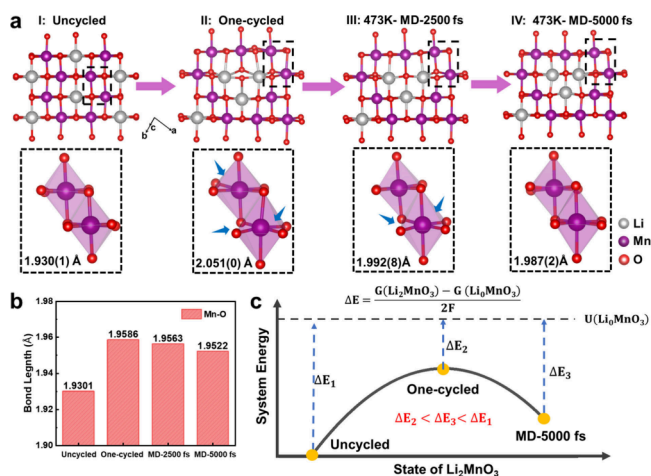


Figure 6. Theoretical calculations to correlate the distortion of TMO₆ octahedra with voltage hysteresis. (a) Optimized structures near the dimerization region of the charged structure extracted from AIMD simulation. Each picture shows the two distorted octahedra within the dotted box of the top structure at different statements, with the average TM–O bonding length indicated below. Notably, the evolution of the average Mn–O bond length in the region near dimerization exhibited pronounced changes, underscoring the severe distortions caused by dimerization. (b) Average Mn–O bond lengths of the optimized structures from AIMD simulation. (c) Diagram to show the relationship between the system energy and average voltage from the equation $\Delta E = [G_{(\text{Li}_2\text{MnO}_3)} - G_{(\text{Li}_0\text{MnO}_3)}]/2F$, where ΔE is the potential difference of a cell formed from the cathode material electrode and standard electrode, $G(Y)$ is the Gibbs energy of the cathode material, and F is Faraday's constant.

and the macroscopic negative thermal expansion. Therefore, we theoretically established the direct link among negative thermal expansion and TMO₆ octahedra distortion, thereby correlating with voltage recovery below 200 °C (0.26 V).

The charging voltage primarily depends on the free energy difference between the charged and pristine states. According to the law of conservation of energy, the substantial voltage hysteresis results in an increase in system energy at the starting state of the second cycle and thus a lower average voltage. This voltage recovery process is exothermic with thermodynamic structural relaxation, leading to a reduction in the internal energy (Figure 6c). Consequently, the increased energy gap between heated discharged Li₂MnO₃ and charged Li₀MnO₃ contributes to the recovery of the charging voltage. This phenomenon elucidates the significant voltage recovery observed after heating and establishes a connection between TMO₆ octahedral distortion and voltage hysteresis.

CONCLUSIONS

In this work, we comprehensively studied the structure evolution during the voltage recovery of one-cycled LMR114 electrodes after undergoing serious voltage hysteresis as a function of the temperature and Li vacancies. Through comprehensive studies into the structural and chemical changes by X-ray spectroscopy, TEM, and temperature-dependent diffraction, a whole exothermic voltage recovery process can be divided into two stages: (1) a large voltage recovery of 0.26 V coupled with an unusual negative thermal expansion below 200 °C; (2) a further recovery of 0.16 V and oxygen plateau through Li-vacancy-assisted reconstruction of Li@Mn₆ superstructure units at 300 °C. These two stages are

strongly correlated with the transition of low-voltage oxygen redox activity to high-voltage oxygen redox activity and subsequently from high-voltage oxygen redox to the oxygen oxidation plateau. While TM migration during stage 2 aligns with the previous investigation, the negative thermal expansion in stage 1 may be surprising and inspiring. This abnormal negative thermal expansion is attributed to the relief of TMO₆ octahedral distortion experimentally and theoretically, which is identified as one of the main factors for voltage recovery. Our findings reveal the presence of two distinct structural variations involved in voltage hysteresis, offering a more comprehensive understanding of the relationship between the lattice structure and voltage behavior in LROs.

METHODS

Electrode Preparation and Electrochemical Measurements

The cathode material, referred to hereafter as LMR114, was supplied by Shenzhen Kejing Star Technology Co. Ltd., China. The electrodes were prepared by blade-casting a slurry composed of 80% active materials, 10% poly(vinylidene difluoride), and 10% carbon black onto aluminum foil and then drying at 80 °C in a vacuum for 12 h. The mass loading of the electrodes was kept at $\sim 3.2 \text{ mg cm}^{-2}$. The 2032-type coin cells were assembled in an argon-filled glovebox with H₂O and O₂ < 0.01 ppm. In the assembly process, the as-prepared electrode was used as the cathode, 600 μm lithium chips served as the anode, and a 60 μL solution of 1 mol of L⁻¹ LiPF₆ in ethylene carbonate/ethyl methyl carbonate (3:7 by weight) was employed as the electrolyte. Galvanostatic charge–discharge testing was carried out using a NEWARE MHWX-200. The cells were charged to 4.8 V vs Li/Li⁺ at 0.1C (1C = 300 mA g⁻¹) and discharged to 2.0 V at 0.1 or 2 C. The cells were disassembled/reassembled in the same glovebox, and subsequent cycling was carried out under the same conditions.

Vacuum Thermal Treatment

After disassembly of the cycled coin cell, the cathodes were picked out and transferred to quartz tubes. The quartz tube was first evacuated to about 5.0×10^{-3} Pa by a vacuum pumper and then sealed by an oxyhydrogen flame. The sealed quartz tube was subjected to heat treatment following the designed temperature profile (heating up to the specific temperature at 5 °C min⁻¹ and holding for 1 h).

Materials Characterization

SEM-EDS characterization was employed using a Zeiss SUPRA 55 scanning electron microscope (Carl Zeiss, Germany). The powder XRD characterizations of LMR powders were carried out using a D8 Discover (Bruker, Germany), and the corresponding crystal refinement was using the GSASII software.³⁰ The ICP tests were conducted by a PE/Avio 220 Max (PerkinElmer, American). The XPS characterization was carried out with a ESCALAB 250Xi X-ray photoelectron spectrometer (Thermo Fisher, American). The DSC test was employed by a DSC1 instrument (Mettler Toledo, Switzerland).

Temperature-Dependent X-ray Diffraction (XRD)

Temperature-dependent XRD patterns were collected using a furnace (Anton Paar HTK-1200N) and a powder X-ray diffractometer (Bruker D8 Advance, Cu K α_1 = 1.54056 Å). The cycled samples were collected from disassembled electrodes and then kept in a quartz plate. After N₂ filled in HTK-1200N, the temperature was increased with 5 °C min⁻¹ until 500 °C.

Varied-Temperature Transmission Electron Microscopy (TEM)

Varied-temperature TEM characterizations were performed in a Titan ETEM G2 with an accelerated voltage of 200 kV. To prepare TEM samples, the cycled sample was dispersed in ethanol and drop-casted onto Cu grids covered with amorphous carbon films. The grid was mounted onto a microelectron-mechanical system based on a

microheater (ThermoFisher Scientific, NanoEx-i/v) and then heated to a specific temperature under high vacuum. Corresponding TEM images were subsequently taken after 1 h of holding at the chosen temperature. To avoid effects from the electron beam on the element distribution dynamics during the *in situ* TEM experiments, we kept the TEM beam off-focus while capturing images.

Soft X-ray Absorption Spectroscopy (sXAS)

sXAS measurements were carried out on Beamline BL02B02 at the Shanghai Synchrotron Radiation Facility. Data were acquired under an ultrahigh vacuum in a single load at room temperature. All samples were scanned from 520 to 554.5 eV in 0.1 eV steps for the O K-edge absorption. Surface-sensitive absorption spectra were recorded using TEY, while bulk-sensitive absorption spectra were recorded using TFY.

Hard X-ray Absorption Spectroscopy (hXAS)

hXAS was collected at the KMC2 beamline of the BESSY II synchrotron at Helmholtz-Zentrum Berlin für Materialien and Energie. Every sample was folded in half and sealed by a polyimide film to ensure the quality of spectra. The spectra were obtained from 8.18 to 8.88 keV for Ni K-edge XAS, from 7.55 to 8.25 keV for Co K-edge XAS, and from 6.38 to 7.08 keV for Mn K-edge XAS. Data analysis and EXAFS fitting were performed with the *Athena* software packages.³¹ Wavelet transform analysis was conducted on the k^3 -weighted normalized EXAFS data for each state of LMR114. The Cauchy wavelet order (n) values were 500, 150, and 250 for Mn, Co, and Ni, respectively.

High-Angle Annular Dark-Field Scanning Transmission Electron Microscopy (HAADF-STEM)

Focused ion beam (FIB)/TEM specimen preparation by FIB liftout was conducted on a FEI Helios NanoLab 600i DualBeam SEM/FIB operating at 2–30 kV. Then the FIB-prepared samples were investigated by using a Titan Cubed Themis G2 300 microscope at 300 kV. The probe convergence angle and the detection angle used for HAADF-STEM imaging were 25 and 64–200 mrad, respectively.

Theoretical Calculation

All of the DFT calculations were performed using the projector-augmented-wave method, as implemented in the Vienna ab initio simulation package (VASP).^{32–34} The Perdew–Burke–Ernzerhof form of the generalized gradient approximation (GGA) was selected to describe the electronic exchange–correlation potential.^{33–35} The spin polarization was taken into consideration. The energy cutoff of planewave was set as 520 eV, and the electronic energy convergence criterion was set as 10^{-5} eV. The Brillouin zone was sampled by Γ -centered Monkhorst–Pack k -point grid with a density of at least 0.2 \AA^{-1} , and for AIMD, a single Γ point was used. Geometries were optimized until the forces on the atoms were less than 0.02 eV \AA^{-1} and less than 0.03 eV \AA^{-1} for CI-NEB calculations. DFT-D3 semiempirical van der Waals correction was applied to deal with the dispersion force during structural relaxation.³⁶ In order to correctly characterize localized TM d electrons, the GGA+ U method was used to account for the strong correlation interactions.^{34,37} The value for the Hubbard U parameter of Mn was 3.9 eV.³⁸ The AIMD simulations were based on the NVT ensemble and Nosé–Hoover thermostat.³⁹ The migration barriers of ions were calculated using the climbing-image nudged elastic band method.⁴⁰

■ ASSOCIATED CONTENT

Data Availability Statement

The data that support the findings of this study are available from the corresponding authors upon reasonable request.

Supporting Information

The Supporting Information is available free of charge at <https://pubs.acs.org/doi/10.1021/acsnano.5c20611>.

Supplementary figures (Figures S1–S27) and tables (Tables S1–S7) on material characterizations (SEM,

HAADF-STEM, XRD, sXAS, etc.), electrochemical tests, and battery performances (PDF)

■ AUTHOR INFORMATION

Corresponding Authors

Jun Wang – School of Innovation and Entrepreneurship, Southern University of Science and Technology, Shenzhen 518055, China; orcid.org/0000-0001-9561-5857; Email: wangj9@sustech.edu.cn

Qi Liu – Department of Physics, City University of Hong Kong, Hong Kong, China; orcid.org/0000-0003-4879-1537; Email: qiliu63@cityu.edu.hk

Mingjian Zhang – School of Science and Engineering, The Chinese University of Hong Kong, Shenzhen 518172, China; orcid.org/0000-0002-6843-5911; Email: zhangmingjian@cuhk.edu.cn

Feng Pan – School of Advanced Materials, Peking University, Shenzhen Graduate School, Shenzhen 518055, China; orcid.org/0000-0002-8216-1339; Email: panfeng@pku.edu.cn

Authors

Haoyu Xue – School of Advanced Materials, Peking University, Shenzhen Graduate School, Shenzhen 518055, China; Shanghai Ideal Automotive Technology Co. Ltd., Shanghai 201800, China

Wenguang Zhao – School of Advanced Materials, Peking University, Shenzhen Graduate School, Shenzhen 518055, China

Minzhi Zhan – School of Advanced Materials, Peking University, Shenzhen Graduate School, Shenzhen 518055, China

Dong Zhou – School of Advanced Energy, Shenzhen Campus of Sun Yat-sen University, Shenzhen 518107, P. R. China

Nian Zhang – Shanghai Synchrotron Radiation Facility, Shanghai Advanced Research Institute, Chinese Academy of Sciences, Shanghai 201204, China; orcid.org/0000-0002-9124-6553

Zhefeng Chen – School of Advanced Materials, Peking University, Shenzhen Graduate School, Shenzhen 518055, China

Rui Qi – Department of Materials, University of Oxford, OX1 3PH Oxford, United Kingdom

Mihai Chu – Department of Chemistry Materials and Chemical Engineering, Politecnico di Milano, Milano 20131, Italy

Shunning Li – School of Advanced Materials, Peking University, Shenzhen Graduate School, Shenzhen 518055, China; orcid.org/0000-0002-5381-6025

Complete contact information is available at: <https://pubs.acs.org/doi/10.1021/acsnano.5c20611>

Author Contributions

M.J.Z., F.P., and H.X. conceived the ideas and designed all of the experiments. M.J.Z., F.P., Q.L., and J.W. supervised the project. H.X. performed the electrochemical tests and data processing. W.Z. and J.W. performed the HAADF-STEM and varied-temperature TEM experiments. D.Z. and N.Z. performed the X-ray absorption spectroscopy experiment. M.Z. performed the theoretical calculation. Z.C., S.L., M.C., and R.Q. participated in the discussion of the mechanism and

provided personal insights. H.X., M.J.Z., and Q.L. wrote the paper. All authors discussed the results and reviewed the paper.

Notes

The authors declare no competing financial interest.

ACKNOWLEDGMENTS

This work was financially supported by the National Natural Science Foundation of China (No. 52172175, No. 52102201 and Grant 92472206), The Major Science and Technology Infrastructure Project of Material Genome Big-science Facilities Platform supported by Municipal Development and Reform Commission of Shenzhen, International joint Research Center for Electric Vehicle Power Battery and Materials (No. 2015B01015), Guangdong Key Laboratory of Design and Calculation of New Energy Materials (No. 2017B030301013), Shenzhen Key Laboratory of New Energy Resources Genome Preparation and Testing (No. ZDSYS201707281026184), and City University of Hong Kong 569 (CityU7005612, CityU21307019, CityU7005500, and CityU7020043).

REFERENCES

- (1) Boettcher, S. W.; Oener, S. Z.; Lonergan, M. C.; Surendranath, Y.; Ardo, S.; Brozek, C.; Kempler, P. A. Potentially Confusing: Potentials in Electrochemistry. *ACS Energy Letters* **2021**, *6* (1), 261–266. Hourng, L. W.; Tsai, T. T.; Lin, M. Y. The analysis of energy efficiency in water electrolysis under high temperature and high pressure. *IOP Conference Series: Earth and Environmental Science* **2017**, *93* (1), 012035.
- (2) Choi, D.; Wang, D.; Bae, I.-T.; Xiao, J.; Nie, Z.; Wang, W.; Viswanathan, V. V.; Lee, Y. J.; Zhang, J.-G.; Graff, G. L.; et al. LiMnPO₄ Nanoplate Grown via Solid-State Reaction in Molten Hydrocarbon for Li-Ion Battery Cathode. *Nano Lett.* **2010**, *10* (8), 2799–2805. Lu, Z.; Chen, H.; Robert, R.; Zhu, B. Y. X.; Deng, J.; Wu, L.; Chung, C. Y.; Grey, C. P. Citric Acid- and Ammonium-Mediated Morphological Transformations of Olivine LiFePO₄ Particles. *Chem. Mater.* **2011**, *23* (11), 2848–2859.
- (3) Masquelier, C.; Croguennec, L. Polyanionic (Phosphates, Silicates, Sulfates) Frameworks as Electrode Materials for Rechargeable Li (or Na) Batteries. *Chem. Rev.* **2013**, *113* (8), 6552–6591.
- (4) Goodenough, J. B.; Park, K.-S. The Li-Ion Rechargeable Battery: A Perspective. *J. Am. Chem. Soc.* **2013**, *135* (4), 1167–1176.
- (5) Liu, C.; Neale, Z. G.; Cao, G. Understanding electrochemical potentials of cathode materials in rechargeable batteries. *Mater. Today* **2016**, *19* (2), 109–123.
- (6) Yu, W.; Li, C.; Li, Y.; Yan, J.; Yu, H.; Zhou, X.; Ma, Y.; Kan, H.; Meng, Q.; Dong, P. Research progress on lithium-rich cathode materials for high energy density lithium-ion batteries. *J. Alloys Compd.* **2024**, *986*, 174156.
- (7) Godshall, N. A.; Raistrick, I. D.; Huggins, R. A. Relationships among Electrochemical, Thermodynamic, and Oxygen Potential Quantities in Lithium-Transition Metal-Oxygen Molten Salt Cells. *J. Electrochem. Soc.* **1984**, *131* (3), 543.
- (8) Csernica, P. M.; McColl, K.; Busse, G. M.; Lim, K.; Rivera, D. F.; Shapiro, D. A.; Islam, M. S.; Chueh, W. C. Substantial oxygen loss and chemical expansion in lithium-rich layered oxides at moderate delithiation. *Nat. Mater.* **2025**, *24* (1), 92–100.
- (9) Singer, A.; Zhang, M.; Hy, S.; Cela, D.; Fang, C.; Wynn, T. A.; Qiu, B.; Xia, Y.; Liu, Z.; Ulvestad, A.; et al. Nucleation of dislocations and their dynamics in layered oxide cathode materials during battery charging. *Nature Energy* **2018**, *3* (8), 641–647.
- (10) Li, Y.; Zuba, M. J.; Bai, S.; Lebens-Higgins, Z. W.; Qiu, B.; Park, S.; Liu, Z.; Zhang, M.; Piper, L. F. J.; Meng, Y. S. Regeneration of degraded Li-rich layered oxide materials through heat treatment-induced transition metal reordering. *Energy Storage Materials* **2021**, *35*, 99–107.
- (11) Sigel, F.; Schwarz, B.; Kleiner, K.; Dräger, C.; Esmezjan, L.; Yavuz, M.; Indris, S.; Ehrenberg, H. Thermally Induced Structural Reordering in Li- and Mn-Rich Layered Oxide Li Ion Cathode Materials. *Chem. Mater.* **2020**, *32* (3), 1210–1223.
- (12) House, R. A.; Rees, G. J.; Pérez-Osorio, M. A.; Marie, J.-J.; Boivin, E.; Robertson, A. W.; Nag, A.; Garcia-Fernandez, M.; Zhou, K.-J.; Bruce, P. G. First-cycle voltage hysteresis in Li-rich 3d cathodes associated with molecular O₂ trapped in the bulk. *Nature Energy* **2020**, *5* (10), 777–785. House, R. A.; Marie, J.-J.; Pérez-Osorio, M. A.; Rees, G. J.; Boivin, E.; Bruce, P. G. The role of O₂ in O-redox cathodes for Li-ion batteries. *Nature Energy* **2021**, *6* (8), 781–789.
- (13) House, R. A.; Maitra, U.; Perez-Osorio, M. A.; Lozano, J. G.; Jin, L.; Somerville, J. W.; Duda, L. C.; Nag, A.; Walters, A.; Zhou, K. J.; et al. Superstructure control of first-cycle voltage hysteresis in oxygen-redox cathodes. *Nature* **2020**, *577* (7791), 502–508.
- (14) House, R. A.; Playford, H. Y.; Smith, R. I.; Holter, J.; Griffiths, I.; Zhou, K.-J.; Bruce, P. G. Detection of trapped molecular O₂ in a charged Li-rich cathode by Neutron PDF. *Energy Environ. Sci.* **2022**, *15* (1), 376–383.
- (15) Maitra, U.; House, R. A.; Somerville, J. W.; Tapia-Ruiz, N.; Lozano, J. G.; Guerrini, N.; Hao, R.; Luo, K.; Jin, L.; Perez-Osorio, M. A.; et al. Oxygen redox chemistry without excess alkali-metal ions in Na(2/3)[Mg(0.28)Mn(0.72)]O(2). *Nat. Chem.* **2018**, *10* (3), 288–295. Luo, D.; Zhu, H.; Xia, Y.; Yin, Z.; Qin, Y.; Li, T.; Zhang, Q.; Gu, L.; Peng, Y.; Zhang, J.; et al. A Li-rich layered oxide cathode with negligible voltage decay. *Nature Energy* **2023**, *8* (10), 1078–1087.
- (16) McCalla, E.; Abakumov, A. M.; Saubanière, M.; Foix, D.; Berg, E. J.; Rouse, G.; Doublet, M.-L.; Gonbeau, D.; Novák, P.; Van Tendeloo, G.; et al. Visualization of O-O peroxo-like dimers in high-capacity layered oxides for Li-ion batteries. *Science* **2015**, *350* (6267), 1516–1521.
- (17) Qiu, B.; Zhou, Y.; Liang, H.; Zhang, M.; Gu, K.; Zeng, T.; Zhou, Z.; Wen, W.; Miao, P.; He, L.; et al. Negative thermal expansion and oxygen-redox electrochemistry. *Nature* **2025**, *640* (8060), 941–946.
- (18) Meng, X. H.; Lin, T.; Mao, H.; Shi, J. L.; Sheng, H.; Zou, Y. G.; Fan, M.; Jiang, K.; Xiao, R. J.; Xiao, D.; et al. Kinetic Origin of Planar Gliding in Single-Crystalline Ni-Rich Cathodes. *J. Am. Chem. Soc.* **2022**, *144* (25), 11338–11347. Lee, S.; Jin, W.; Kim, S. H.; Joo, S. H.; Nam, G.; Oh, P.; Kim, Y. K.; Kwak, S. K.; Cho, J. Oxygen Vacancy Diffusion and Condensation in Lithium-Ion Battery Cathode Materials. *Angew. Chem., Int. Ed. Engl.* **2019**, *58* (31), 10478–10485. Qian, D.; Xu, B.; Chi, M.; Meng, Y. S. Uncovering the roles of oxygen vacancies in cation migration in lithium excess layered oxides. *Phys. Chem. Chem. Phys.* **2014**, *16* (28), 14665–14668.
- (19) Assat, G.; Foix, D.; Delacourt, C.; Iadecola, A.; Dedryvère, R.; Tarascon, J.-M. Fundamental interplay between anionic/cationic redox governing the kinetics and thermodynamics of lithium-rich cathodes. *Nat. Commun.* **2017**, *8* (1), 2219. Gent, W. E.; Lim, K.; Liang, Y.; Li, Q.; Barnes, T.; Ahn, S.-J.; Stone, K. H.; McIntire, M.; Hong, J.; Song, J. H.; et al. Coupling between oxygen redox and cation migration explains unusual electrochemistry in lithium-rich layered oxides. *Nat. Commun.* **2017**, *8* (1), 2091.
- (20) Barrera, G. D.; Bruno, J. A. O.; Barron, T. H. K.; Allan, N. L. Negative thermal expansion. *J. Phys.: Condens. Matter* **2005**, *17* (4), R217. Li, Q.; Lin, K.; Liu, Z.; Hu, L.; Cao, Y.; Chen, J.; Xing, X. Chemical Diversity for Tailoring Negative Thermal Expansion. *Chem. Rev.* **2022**, *122* (9), 8438–8486.
- (21) Rimmer, L. H. N.; Dove, M. T.; Winkler, B.; Wilson, D. J.; Refson, K.; Goodwin, A. L. Framework flexibility and the negative thermal expansion mechanism of copper(I) oxide Cu₂O. *Phys. Rev. B* **2014**, *89* (21), 214115.
- (22) Li, Q.; Qiao, R.; Wray, L. A.; Chen, J.; Zhuo, Z.; Chen, Y.; Yan, S.; Pan, F.; Hussain, Z.; Yang, W. Quantitative probe of the transition metal redox in battery electrodes through soft x-ray absorption spectroscopy. *J. Phys. D: Appl. Phys.* **2016**, *49* (41), 413003.
- (23) Csernica, P. M.; Kalirai, S. S.; Gent, W. E.; Lim, K.; Yu, Y.-S.; Liu, Y.; Ahn, S.-J.; Kaeli, E.; Xu, X.; Stone, K. H.; et al. Persistent and partially mobile oxygen vacancies in Li-rich layered oxides. *Nature*

Energy **2021**, *6* (6), 642–652. Wen, B.; Sayed, F. N.; Dose, W. M.; Morzy, J. K.; Son, Y.; Nagendran, S.; Ducati, C.; Grey, C. P.; De Volder, M. F. L. Surface reduction in lithium- and manganese-rich layered cathodes for lithium ion batteries drives voltage decay. *Journal of Materials Chemistry A* **2022**, *10* (41), 21941–21954.

(24) Luo, K.; Roberts, M. R.; Hao, R.; Guerrini, N.; Pickup, D. M.; Liu, Y.-S.; Edström, K.; Guo, J.; Chadwick, A. V.; Duda, L. C.; et al. Charge-compensation in 3d-transition-metal-oxide intercalation cathodes through the generation of localized electron holes on oxygen. *Nat. Chem.* **2016**, *8* (7), 684–691.

(25) Chen, Z.; Chevrier, D. M.; Conn, B. E.; Bigioni, T. P.; Zhang, P. Utilizing an Improved EXAFS Structure Analysis Method to Reveal Site-Specific Bonding Properties of Ag₄₄(SR)₃₀ Nanoclusters. *J. Phys. Chem. C* **2023**, *127* (42), 20771–20778.

(26) Sayers, D. E.; Stern, E. A.; Lytle, F. W. New Technique for Investigating Noncrystalline Structures: Fourier Analysis of the Extended X-Ray—Absorption Fine Structure. *Phys. Rev. Lett.* **1971**, *27* (18), 1204–1207. Rehr, J. J.; Albers, R. C. Theoretical approaches to x-ray absorption fine structure. *Rev. Mod. Phys.* **2000**, *72* (3), 621–654.

(27) Jing, C.; Liu, S.; Patel, M.; Meng, X. Arsenic Leachability in Water Treatment Adsorbents. *Environ. Sci. Technol.* **2005**, *39* (14), 5481–5487.

(28) Muñoz, M.; Argoul, P.; Farges, F. o. Continuous Cauchy wavelet transform analyses of EXAFS spectra: A qualitative approach. *Am. Mineral.* **2003**, *88* (4), 694–700.

(29) Li, B.; Sougrati, M. T.; Rousse, G.; Morozov, A. V.; Dedryvere, R.; Iadecola, A.; Senyshyn, A.; Zhang, L.; Abakumov, A. M.; Doublet, M. L.; et al. Correlating ligand-to-metal charge transfer with voltage hysteresis in a Li-rich rock-salt compound exhibiting anionic redox. *Nat. Chem.* **2021**, *13* (11), 1070–1080.

(30) Toby, B. H.; Von Dreele, R. B. GSAS-II: the genesis of a modern open-source all purpose crystallography software package. *J. Appl. Crystallogr.* **2013**, *46* (2), 544–549.

(31) Ravel, B.; Newville, M. ATHENA, ARTEMIS, HEPHAESTUS: data analysis for X-ray absorption spectroscopy using IFEFFIT. *Journal of synchrotron radiation* **2005**, *12* (4), 537–541.

(32) Kresse, G.; Furthmüller, J. Efficiency of ab-initio total energy calculations for metals and semiconductors using a plane-wave basis set. *Comput. Mater. Sci.* **1996**, *6* (1), 15–50.

(33) Blöchl, P. E. Projector augmented-wave method. *Phys. Rev. B* **1994**, *50* (24), 17953–17979.

(34) Perdew, J. P.; Burke, K.; Ernzerhof, M. Generalized Gradient Approximation Made Simple. *Phys. Rev. Lett.* **1996**, *77* (18), 3865–3868.

(35) Kresse, G.; Joubert, D. From ultrasoft pseudopotentials to the projector augmented-wave method. *Phys. Rev. B* **1999**, *59* (3), 1758–1775.

(36) Grimme, S.; Antony, J.; Ehrlich, S.; Krieg, H. A consistent and accurate ab initio parametrization of density functional dispersion correction (DFT-D) for the 94 elements H-Pu. *J. Chem. Phys.* **2010**, *132* (15), 154104.

(37) Dudarev, S. L.; Botton, G. A.; Savrasov, S. Y.; Humphreys, C. J.; Sutton, A. P. Electron-energy-loss spectra and the structural stability of nickel oxide: An LSDA+U study. *Phys. Rev. B* **1998**, *57* (3), 1505–1509. Anisimov, V. I.; Zaanen, J.; Andersen, O. K. Band theory and Mott insulators: Hubbard U instead of Stoner I. *Phys. Rev. B* **1991**, *44* (3), 943–954.

(38) Wang, L.; Maxisch, T.; Ceder, G. Oxidation energies of transition metal oxides within the GGA+U framework. *Phys. Rev. B* **2006**, *73* (19), 195107.

(39) Nosé, S. A unified formulation of the constant temperature molecular dynamics methods. *J. Chem. Phys.* **1984**, *81* (1), 511–519. Hoover, W. G. Canonical dynamics: Equilibrium phase-space distributions. *Phys. Rev. A* **1985**, *31* (3), 1695–1697.

(40) Henkelman, G.; Uberuaga, B. P.; Jónsson, H. A climbing image nudged elastic band method for finding saddle points and minimum energy paths. *J. Chem. Phys.* **2000**, *113* (22), 9901–9904.

(41) Chen, Z.; Li, J.; Zeng, X. C. Unraveling Oxygen Evolution in Li-Rich Oxides: A Unified Modeling of the Intermediate Peroxo/Superoxo-like Dimers. *J. Am. Chem. Soc.* **2019**, *141* (27), 10751–10759.



CAS BIOFINDER DISCOVERY PLATFORM™

**PRECISION DATA
FOR FASTER
DRUG
DISCOVERY**

CAS BioFinder helps you identify targets, biomarkers, and pathways

Unlock insights

CAS
A Division of the
American Chemical Society